

# Processing–Morphology–Property Relationships and Composite Theory Analysis of Reduced Graphene Oxide/Natural Rubber Nanocomposites

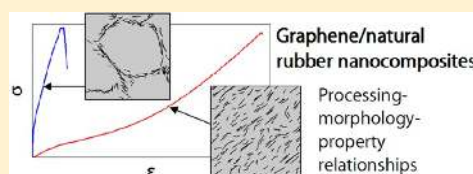
Jeffrey R. Potts,<sup>†</sup> Om Shankar,<sup>†</sup> Ling Du,<sup>‡</sup> and Rodney S. Ruoff<sup>\*,†</sup>

<sup>†</sup>Department of Mechanical Engineering and the Materials Science and Engineering Program, The University of Texas at Austin, 204 E. Dean Keeton St., Austin, Texas 78712, United States

<sup>‡</sup>Goodyear Tire and Rubber Company, 142 Goodyear Boulevard, Akron, Ohio 44305, United States

## S Supporting Information

**ABSTRACT:** Dispersion of reduced graphene oxide (RG-O) into natural rubber (NR) was found to dramatically enhance the mechanical, electrical, and thermal properties of NR. However, property improvements were strongly dependent upon the processing history and nanocomposite morphology. Co-coagulating a stable RG-O suspension with NR latex afforded a weblike morphology consisting of platelet networks between the latex particles, while two-roll mill processing broke down this structure, yielding a homogeneous and improved dispersion. The physical properties of RG-O/NR vulcanizates with both morphologies were compared over a range of loadings; it was found that the network morphology was highly beneficial for thermal and electrical conductivity properties and greatly increased stiffness but was detrimental to elongation. A detailed comparative analysis of composite models found the Guth equation gave excellent fit to modulus data of the milled samples when taking the shape factor as equal to the platelet aspect ratio quantified from transmission electron microscopy analysis.



## 1. INTRODUCTION

To meet the demands of many critical applications, elastomers are blended with particulate fillers. Fillers are typically added to elastomers to improve properties such as strength and abrasion resistance, but they can also be used to enhance the electrical and thermal conductivity and permeability resistance of a rubber compound. Over the past two decades, the blending of nanomaterials—such as exfoliated layered silicates and carbon nanotubes—into elastomers has been explored in detail, with the goal of supplementing or replacing conventional fillers such as carbon black and silica.<sup>1</sup> The excellent physical properties, high surface area, and anisotropy (aspect ratio) of many nanomaterials suggest tremendous promise for use as fillers for elastomers and polymers more generally.<sup>2</sup>

Given the recent development of graphene-based materials produced by scalable chemical routes, it is of significant interest to establish effective dispersion techniques for and investigate the use of graphene-based materials for elastomer reinforcement. To date, however, only a small fraction of the large body of literature on graphene/polymer nanocomposites has investigated graphene-filled elastomers.<sup>3–5</sup> Very little work has examined property enhancement in nonpolar rubbers such as natural rubber (NR) which are of significant technological interest. Just as with thermoplastic–matrix nanocomposites,<sup>2</sup> elastomeric nanocomposites can be produced by three general routes: melt compounding, *in situ* polymerization, and solution/latex mixing. Considering the ease by which kinetically stable aqueous suspensions of graphene-based materials can be

made,<sup>6–8</sup> latex mixing could provide an effective means for production of graphene/rubber nanocomposites.

Latex mixing and co-coagulation have been extensively studied with layered silicate/rubber nanocomposite systems.<sup>1</sup> Yu and co-workers performed the earliest studies on latex compounding of rubber latices with pristine clay/water suspensions,<sup>9,10</sup> first demonstrating the performance advantage of high aspect ratio nanoclays over carbon black. Others expanded on this work by examining the morphological characteristics of co-coagulated clay/rubber hybrids and concluded that co-coagulation excludes the possibility of an “intercalated” morphology, leading only to restacked or exfoliated platelets<sup>11</sup> while generating a “house of cards” morphology consisting of networks of nanoclay platelets confined within the interstices of the coagulated latex particles.<sup>12</sup> Further studies have examined the effect of processing variables on the morphology and properties of latex compounded nanoclay/rubber composites, including the use of different coagulation agents and/or drying conditions<sup>13,14</sup> to improve filler dispersion and compound properties.

An analogous latex co-coagulation approach using graphene platelet suspensions could be expected to yield similar results since both exfoliated montmorillonite and graphene platelets are high aspect ratio platelets, although graphene-based materials tend to show more crumpled conformations when

Received: April 5, 2012

Revised: June 26, 2012

Published: July 19, 2012

dispersed in a polymer.<sup>2</sup> Recently, Zhan and co-workers published a study on reduced graphene oxide/natural rubber nanocomposites fabricated by an ultrasonically assisted latex mixing masterbatch technique.<sup>5</sup> Their findings illustrated the tremendous potential of graphene in natural rubber reinforcement. However, their production method involved hydrazine reduction of a graphene oxide suspension without the aid of electronic or steric stabilization, which likely caused significant flocculation and restacking of the reduced graphene oxide platelets prior to mixing which would be detrimental to the filler dispersion. Moreover, their work considered nanocomposites only up to 2 wt %, and it is of interest to evaluate the performance of nanocomposites at higher filler loadings.

In this work, the production of reduced graphene oxide/natural rubber (NR) nanocomposites by a related latex co-coagulation method is described, which begins with preparation of a kinetically stable dispersion of single-layer reduced graphene oxide (RG-O) platelets. It was expected that the co-coagulation process would afford a “skeleton” or network morphology based upon the work described previously.<sup>12</sup> However, we sought to investigate what benefit to composite properties, if any, such a morphology offers relative to a more uniform, homogeneous, and well-exfoliated dispersion—the oft-cited goal in nanocomposites research. Such a consideration would also be relevant from a technological perspective. For example, latex co-coagulated nanocomposites would not likely be used directly in typical applications but would instead be utilized as a masterbatch compound which would be diluted or otherwise mixed to some extent using, for example, a two-roll mill or internal mixer.<sup>1</sup> The intense shear forces generated by these mixing operations would be expected to destroy the network morphology created by co-coagulation. Differences in the property trends between the two types of nanocomposites could also be analyzed with simple composite models to gain additional insight. Thus, the goal of this paper is thus to explore the effect of the milling process on the morphology and properties of latex co-coagulated NR/RG-O nanocomposites and also to examine these results within the context of composite theory.

## 2. EXPERIMENTAL METHODS

### Preparation of Reduced Graphene Oxide Suspensions.

Reduced graphene oxide (RG-O) filler was produced by exfoliation of graphite oxide (GO). GO was synthesized by oxidation of purified natural flake graphite (SP-1, Bay Carbon) by a modified Hummers method. In this process, 12 g of graphite was added to 600 mL of concentrated  $\text{H}_2\text{SO}_4$ , and then 50 g of  $\text{KMnO}_4$  was slowly added over an ice bath. The reaction mixture was stirred at room temperature for 24 h and then put back on an ice bath, and then ~1500 mL of deionized water was slowly added and  $\text{H}_2\text{O}_2$  (30%) was added until the mixture became orange/gold in color. GO (a yellow-brown solid) was isolated by vacuum filtration and dried; the yield of GO from this procedure was approximately 22–25 g.

Aqueous colloidal suspensions of graphene oxide (G-O) were produced by exfoliation of GO. 500 mg of GO was added to 750 mL of water and treated in an ultrasonic bath (VWR, 97043-968) for 4 h and stirred for at least 24 h (until no turbidity was present in the mixture). Individual batches were produced in this manner and combined into larger batches for reduction. In a typical procedure, individual G-O suspensions were combined into a 3 L round-bottom flask, and the pH was adjusted to ~11.5 using potassium hydroxide. Then, hydrazine monohydrate ( $\text{N}_2\text{H}_4\cdot\text{H}_2\text{O}$ ) in an amount equal to 1  $\mu\text{L}$  per 1 mg of GO was added to the flask, which was allowed to stir for 48 h at 30 °C to produce a kinetically stable suspension of RG-O platelets in water.

As some mass is lost from G-O platelets upon reduction, it was desired to quantify this loss in order to determine the proper mass of GO to use to achieve a desired loading of RG-O platelets in the nanocomposites. For this step, an aqueous RG-O suspension produced from 500 mg of GO was coagulated with formic acid, then filtered, dried, and weighed. This procedure was performed twice, giving an average ratio of RG-O to GO mass of 0.61. Thus, for mixing calculations, the required mass of RG-O to achieve a certain loading was calculated, and that number was then divided by 0.61 to get the amount of GO needed for that nanocomposite batch.

**Nanocomposite Mixing, Coagulation, Treatment, and Processing.** A latex co-coagulation procedure was used to produce the nanocomposites. Natural rubber (NR) latex supplied by Goodyear Tire & Rubber Company with a solids fraction of 61% was weighed in calculated amounts to produce nanocomposites at specific loading intervals corresponding to 2, 3, 4, and 5 wt % RG-O platelets. The RG-O suspension and NR latex were added to a beaker and stirred vigorously for 5 min until the mixture appeared homogeneous. Co-coagulation was induced by rapid addition of 10% v/v formic acid solution. The solid(s) formed upon coagulation was isolated by vacuum filtration and dried.

Following the co-coagulation procedure, the composites were processed by two different routes to incorporate curing agent and investigate the effect of processing on morphology. One set of composites was worked on a two-roll mill (two-roll Prep-Mill, 4 in.  $\times$  8 in. rolls, CW Brabender Instruments). The rolls were set to a temperature of ~80 °C, a speed of 15 rpm with a friction ratio of 1.3:1, and a nip gap of 1 mm. The milling time for each batch was ~12 min. Dicumyl peroxide (DCP; 98%, Aldrich) was used as the curing agent and added at a concentration of 1 phr (part per hundred rubber), unless otherwise specified (see section 5). For each batch, ~50 g of rubber or composite was used to allow the rubber to band over the rolls, while the temperature was adjusted to create an elastic band (i.e., no crumbling/tearing of the banded compound) over the front roll in an attempt to provide the best dispersion possible.<sup>15</sup> In addition, a neat NR control batch was prepared using the same milling conditions.

The remainder of the nanocomposites were processed in a manner as to preserve the morphology created by the co-coagulation process. In this procedure, which will henceforth be referred to as the “solution treatment” procedure, the solids (in the form of small pellets) were soaked for 24 h in a solution of DCP in toluene to swell the rubber and implant DCP into the matrix. Unless otherwise specified (see Supporting Information), 1 phr of DCP was added to the minimal amount of toluene which immersed the pellets completely. After the rubber was completely swollen by the DCP/toluene mixture, the toluene was then removed by vacuum drying for 1 week at room temperature.

Hot pressing was used to form and cure samples for testing (Wabash hydraulic press, 50-1512-2TM). Except where otherwise specified, the samples were cured at 150 °C for 60 min under a 40 kip load. The optimum curing time/temperature was determined by trial and error based upon literature precedent, as described at length in the Supporting Information. For comparison, uncured nanocomposite pellets were loaded into molds and pressed for 15 min at 150 °C and 40 kip to form parts for testing.

**Morphological Characterization.** Transmission electron microscopy (TEM), scanning electron microscopy (SEM), and wide-angle X-ray scattering (WAXS) were used to characterize nanocomposite morphology. For TEM imaging, thin sections (~70 nm) of composite were cut using a cryoultramicrotome (Leica Inst., DiATOME cryo 35° diamond blade) with a –120 °C chamber temperature and a knife temperature of –95 °C. Sections were collected onto 300 mesh Gilder grids from Ted Pella. TEM digital micrographs were acquired using a JEOL 2010F at 200 kV. SEM images were obtained using an FEI Quanta-600 FEG Environmental SEM at 20 kV and  $10^{-6}$  Torr. X-ray scattering was performed on a Philips X-PERT diffractometer using Cu  $K\alpha$  radiation, a generating voltage of 40 kV, a current of 30 mA, and a 2 s dwell time.

**Stress–Strain Testing and Dynamic Mechanical Analysis.** Uniaxial tensile testing was performed at room temperature with an

MTS machine equipped with a 25 lb Honeywell load cell and spring-loaded clamps to prevent slippage of the specimens during testing. Data were acquired using LabVIEW. Samples were “dog-bone” shaped with approximate test section dimensions of  $20 \times 4 \times 1$  mm. Milled samples were stretched three times to an elongation of 200% prior to testing to correct for stress softening (Mullins effect<sup>16</sup>); green and solution treated samples were not prestrained prior to testing due to their low elongations to break. The strain rate for all tests was 250 mm/min unless otherwise noted. Dynamic mechanical analysis (DMA) was performed using a TA Instruments Q800 DMA. All tests were conducted at 10 Hz from  $-100$  to  $50$  °C with a ramp rate of  $2$  °C/min, a strain of 0.1% to 1% (depending on loading), and a static preload of 0.01 N. Samples had dimensions of approximately  $15 \times 5 \times 1$  mm.

**Thermal and Electrical Conductivity Testing.** Electrical conductivity measurements were made using a HIOKI Ultramega ohmmeter (SM-8220) with a HIOKI SM-8000 series electrode and enclosure. Volumetric and surface resistivity measurements were made with this instrument and used to determine the volumetric and surface conductivities, respectively. The electrical conductivity of the highly conductive samples was measured with a Keithley 2410 electrometer, connected to the same HIOKI enclosure. Thermal conductivity was tested using a transient “hot disk” method to measure the in-plane conductivity (measurements performed by Goodyear Tire & Rubber Company). The thermal conductivity was calculated from the density, specific heat, and thermal diffusivity of the material as measured. Samples for electrical conductivity measurements were disk-shaped and  $\sim 1$  mm thick with a surface area (of one face) of at least  $1$  cm<sup>2</sup>. Thermal conductivity samples measured  $51$  mm  $\times$   $51$  mm  $\times$   $6.4$  mm.

### 3. LATEX MIXING AND CO-COAGULATION PROCESS

Latex mixing and co-coagulation is a process analogous to the solution mixing procedure commonly described in the literature, except polymer latex is used instead of a polymer solution. NR latex consists of latex particles ranging from 100 nm to  $2$   $\mu$ m in diameter (see Supporting Information for SEM images of latex particles). The pH of the as-received NR latex was 10.6; thus, addition of the latex to the alkaline RG-O suspension did not lead to coagulation of the suspension. After the NR latex and RG-O suspension were mixed together to form a mixture with a homogeneous appearance, dilute formic acid solution was added to the mixture to drive co-coagulation. Acid causes both the latex particles and the RG-O platelets to coagulate simultaneously. As a result, some of the single-layer RG-O platelets may restack to form multilayer RG-O tactoids upon coagulation; our observations support the intuitive notion that it becomes more likely for platelets to restack as the RG-O content increases in the mixture (i.e., the loading increases). No attempt was made to optimize the coagulation process or study the effect (if any) of different coagulants and speed of addition of coagulant on morphology and properties. Rather, acid solution was added rapidly to the mixture, following the argument of Wu and co-workers.<sup>11</sup>

Following addition of the formic acid solution to the mixture, complete coagulation appeared to occur over a time scale of  $\sim 10$  s. For nominal RG-O loadings of 6 wt % and lower, the supernatant remaining after coagulation was clear and colorless. If the loading of RG-O was increased further, then the supernatant would appear cloudier and slightly gray in color. At 10 wt % nominal loading of RG-O, it was evident that the flocculation of RG-O platelets was occurring more rapidly than coagulation of the NR latex particles, as some NR latex would coagulate separately from the composite, resulting in a “salt and pepper” appearance to the coagulated solid. The form of the coagulated solid also changed with RG-O loading. When neat NR latex was coagulated, the latex particles clumped together to

form a single, large mass of rubber. As the loading of RG-O was increased, the solids became pellet-shaped and gradually decreased in size ( $\sim 1$  mm in diameter at 5 wt %). At 10 wt %, the coagulated solid took on a similar appearance to flocculated RG-O platelets, the coagulated solid consisting of millimeter-size small particles.

### 4. NANOCOMPOSITE MORPHOLOGY

WAXS was used to assess the state of dispersion by comparing scattering patterns of the nanocomposites with those of neat NR. Comparing the spectra of the solution treated nanocomposites at various loadings, a slight shoulder corresponding approximately to the interlayer spacing of graphite (0.34 nm) emerged at 5 wt % which became particularly pronounced by 10 wt %, suggesting the presence of a significant concentration of multilayer tactoids (see Figure S.1). WAXS was also used to compare the state of dispersion between the solution-treated and milled nanocomposites. Close inspection of Figure 1 reveals that the presence of this shoulder in the spectrum is diminished following the milling process, indicating that milling improves the dispersion of filler to some extent.

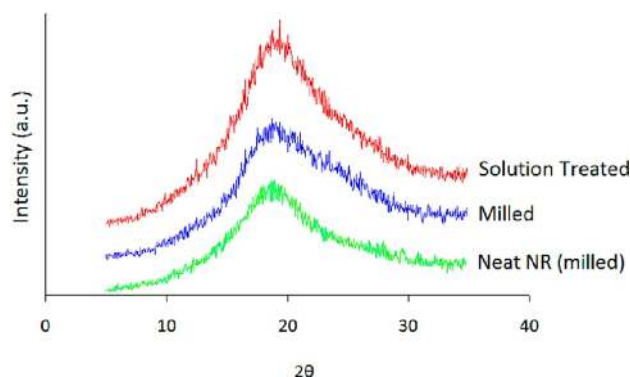


**Figure 1.** Comparison of WAXS spectra of neat NR, milled RG-O/NR, and solution-treated RG-O/NR nanocomposites with 5 wt % RG-O platelets.

TEM was also used to examine the dispersion of the nanocomposites. Figure 2a,b shows representative micrographs from uncured nanocomposite samples. The images show a nonuniform particle density over the cross section, with sub-micrometer regions void of particles surrounded by areas of high particle density. It is speculated that the regions void of reduced graphene oxide platelets correspond to the locations of a latex particle or clumps of particles (see Figure S.6 for latex particle SEM images)—evidently, the hot pressing procedure appears to preserve the morphology created by the co-coagulation procedure. A similar morphology has been achieved by latex co-coagulation of layered silicates and natural rubber. For example, Varghese and Karger-Kocsis identified a “skeleton” structure via TEM following co-coagulation of sodium montmorillonite with NR latex (though they processed composites via solution casting, rather than hot pressing).<sup>12</sup> A significant concentration of multilayer tactoids are clearly visible in some of the micrographs, which is likely due to restacking of the platelets during the coagulation process. It should be noted that thicker tactoids were more prevalent at 5 wt % than at 3 wt % (see TEM micrographs in the Supporting Information), suggesting that the higher the ratio of NR latex to RG-O



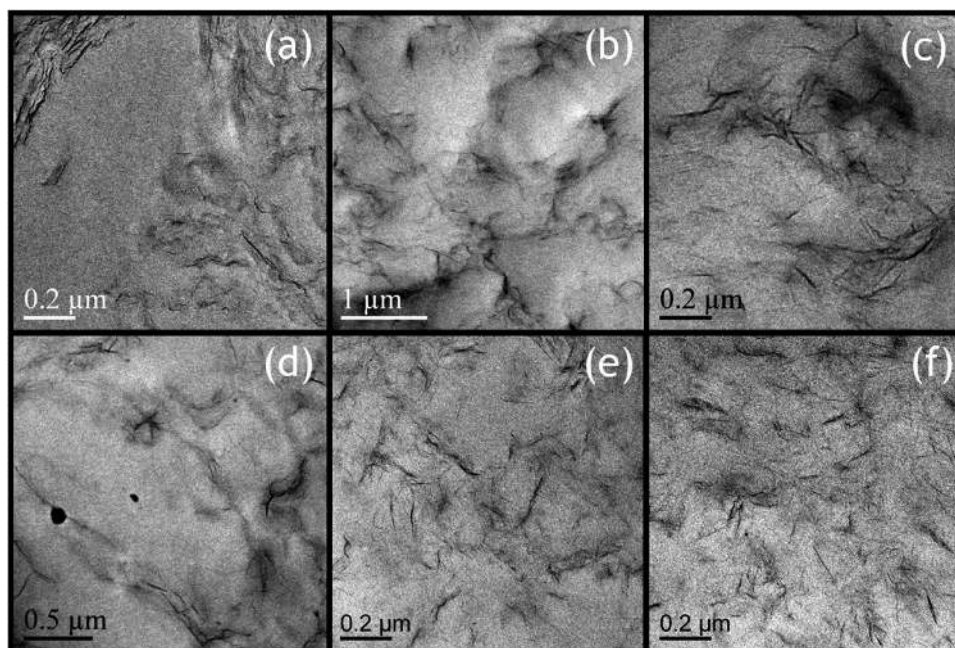


**Figure 2.** TEM micrographs of RG-O/NR nanocomposite sections. Images (a) and (b) show the “weblike” dispersion of RG-O platelets in the uncured composites, as obtained directly after latex co-coagulation. Images (c) and (d) show the dispersion in the solution-treated samples, while images (e) and (f) show the morphology of the milled nanocomposites.

platelets, the greater the likelihood that a latex particle would interrupt the flocculation and restacking of the RG-O platelets.

Images (c) and (d) in Figure 2 are micrographs of RG-O/NR vulcanizates processed by solution treatment. The strong resemblance of the morphology to the micrographs of Figure 2a,b suggests that the morphology created by latex co-coagulation is preserved if the peroxide curing agent is implanted into the rubber by solution treatment (i.e., swelling of the rubber matrix does not appreciably affect the filler morphology). Images (e) and (f) are micrographs of RG-O/NR nanocomposites which were worked on the two-roll mill. It is evident that the segregated “weblike” morphology created by latex co-coagulation is destroyed by the milling process. The platelets are much more uniformly distributed over the cross section and appear highly disoriented, as evidenced by the dark gray regions around the black platelet edges. Perhaps surprisingly, a significant amount of platelet disorientation was observed in the milled nanocomposites, despite the intense shear forces generated in the nip of a two-roll mill that would be expected to orient the platelets along a common axis.

Quantitative analysis of representative TEM micrographs of the solution-treated and milled nanocomposites indicate a better dispersion for the milled compounds, with a slightly higher number-average aspect ratio in the milled sample of roughly 44 versus 41 for the green samples. Significantly fewer low aspect ratio platelets were observed in the milled samples (see Figure 11; more details on the analysis and quantification procedure are provided in section 8). Thus, two-roll mill processing appears to improve the quality and uniformity of the dispersion for latex co-coagulated RG-O/NR nanocomposites.

## 5. ELECTRICAL AND THERMAL CONDUCTIVITY

Differences in nanocomposite morphology had a significant impact on the electrical and thermal conductivity properties. As evident from Figure 3, the solution-treated samples showed a much lower electrical conductivity percolation threshold and

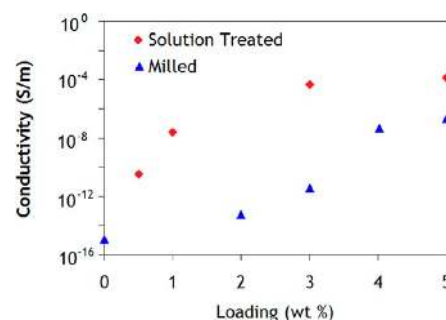


**Figure 3.** Volumetric electrical conductivity of solution-treated and milled RG-O/NR nanocomposites as a function of RG-O loading.

higher electrical conductivity values than the milled samples. These results can be directly attributed to the difference in morphology between the two types of samples. Confinement of RG-O platelets between latex particles promotes a lower effective “percolation threshold” whereby a large increase in nanocomposite conductivity is observed: since the effective volume fraction of the RG-O platelets in the interstitial areas between latex particles is much greater than the nominal volume fraction of the bulk composite, the probability of interparticle contact is significantly greater than the case of statistical percolation of a uniform filler dispersion at an equivalent volume fraction  $\phi$ . The segregated filler networks in the solution treated samples provide more pathways for conduction compared with the milled samples, wherein the well-dispersed platelets are coated with a sheath of polymer which inhibits electrical conduction through the filler network (requiring conduction by tunneling), resulting in lower values of electrical conductivity above the percolation threshold.<sup>17</sup> As shown in the Supporting Information, the conductivity properties of the solution treated nanocomposites are very similar to the green nanocomposites, highlighting the

morphological similarities between the two types of samples observed by TEM.

As observed with the electrical conductivity, the network morphology of the solution-treated composites is beneficial for thermal conductivity enhancement, although the difference in thermal conductivity between the two sample types is far less pronounced. Thermal conductivity results are summarized in Figure 4. At 5 wt %, the measured thermal conductivities of the

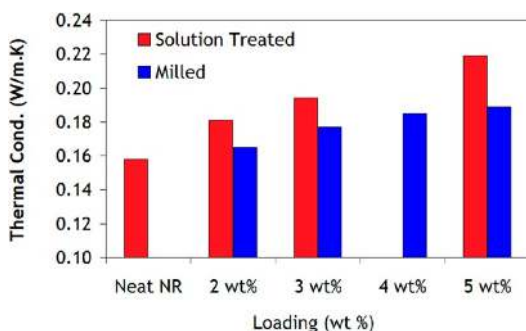


**Figure 4.** Thermal conductivities of milled and solution-treated RG-O/NR nanocomposites at various loadings.

solution treated and milled nanocomposites was 0.219 and 0.188 W/(m K), respectively, compared with 0.157 W/(m K) for neat NR. A slight improvement in thermal stability of NR was observed with incorporation of RG-O as shown in Figure S.11.

## 6. MECHANICAL AND VISCOELASTIC PROPERTIES

Regardless of the processing conditions or cure state, the mechanical properties of NR were altered significantly by the RG-O platelets. Figure 5 illustrates trends in the stress–strain behavior of the solution treated and milled nanocomposites. It should be noted that morphological factors are not entirely responsible for the difference in properties—it is well-known that the milling process breaks down the latex particles and

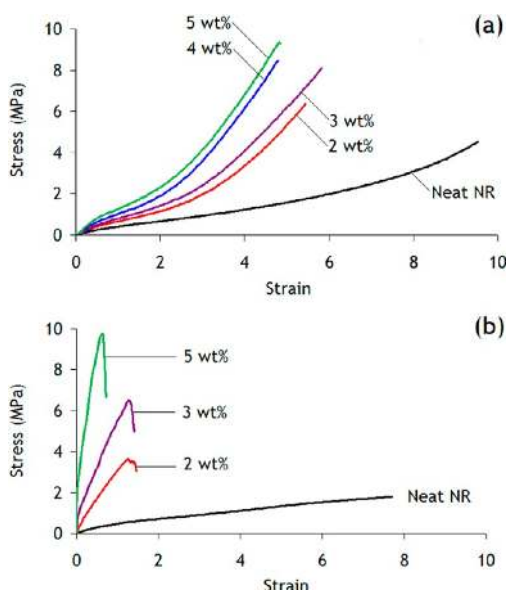


**Figure 5.** Representative stress–strain curves of the (a) milled and (b) solution-treated RG-O/NR nanocomposites showing trends in the stress–strain behavior with filler loading.

lowers the average molecular weight of the chains due to mechanochemical degradation, lowering the modulus of the rubber.<sup>18,19</sup> However, after normalizing composite moduli to each type of control NR specimen (solution-treated or milled), major differences in the property trends were evident between the two types of samples. All nanocomposites showed increased modulus and strength versus neat NR, but the dependence of modulus on RG-O loading was particularly strong for the solution treated samples. It can be seen that the stress–strain behavior of these samples trended toward that of a thermoplastic (Figure 5b), similar to the behavior observed with the uncured nanocomposites shown in Figure S.12. The difference in stiffness between the 5 wt % milled and solution-treated samples is significant enough to be easily detected by hand by stretching or bending the sample.

The stress–strain behavior of the milled RG-O/NR nanocomposites contrasts sharply with that of the solution-treated samples. The stress–strain curves exhibit the sigmoidal shape characteristic of neat and filled NR, showing evidence of strain-induced crystallization at high elongation. Whereas modulus increases in the solution-treated samples were most pronounced at low elongations, the reinforcement effect of RG-O platelets is most pronounced at high elongations in the milled samples. For milled samples, the strain at break was still found to decrease as the loading of RG-O was increased; however, the decrease was much less pronounced than with the solution-treated samples. The milled samples showed an average strain at break of 4.26 at 5 wt %, compared with 0.61 for the 5 wt % solution-treated samples—less than the amount of strain sometimes used to define a rubber (greater than 1)<sup>20</sup>—representing a 49% and 90% decrease in elongation versus neat NR, respectively.

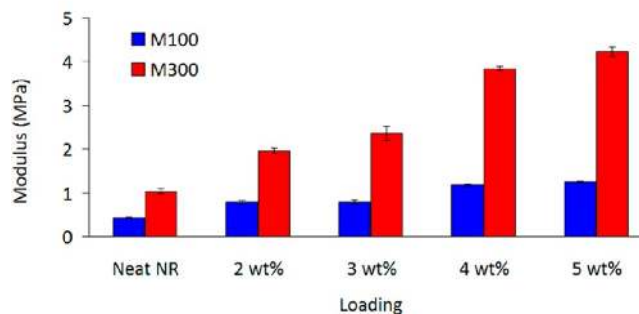


**Figure 6.** Variation in modulus at 100% elongation (M100) and 300% elongation (M300) with loading for milled RG-O/NR nanocomposites.

Figures 6 and 7 summarize results from the tests. Initial (elastic) modulus, modulus at 100% elongation (M100), modulus at 300% elongation (M300), tensile strength, and elongation at break were determined at various loadings according to ASTM D412. Because of the low elongations to break, M100 and M300 were not determined for the solution-treated samples. Figure 7 compares the strength and strain to break of the solution-treated and milled nanocomposites, emphasizing the trends evident from the stress–strain graphs of Figure 5. The low elongations to break observed with the solution treated composites translated to a significantly lower fracture toughness (energy to break) compared to the milled compounds. For both sets of composites, no significant

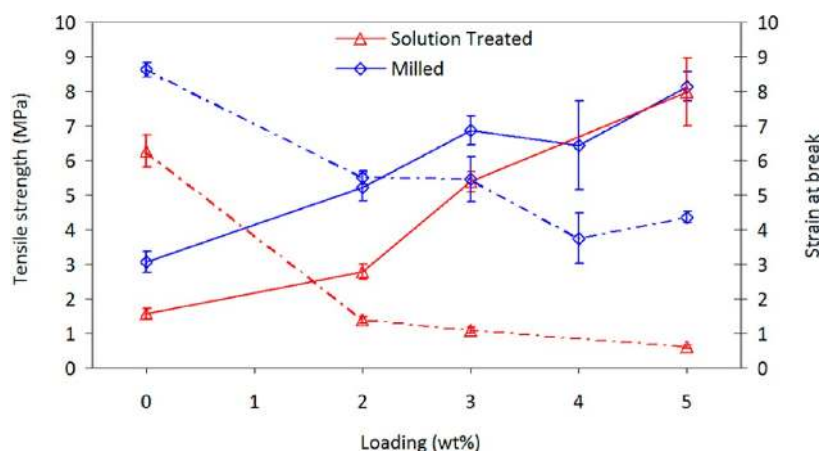


**Figure 7.** Comparison of tensile strength and strain at break between milled and solution-treated RG-O/NR nanocomposites. Solid lines correspond to strength data, and dashed lines indicate elongation data.

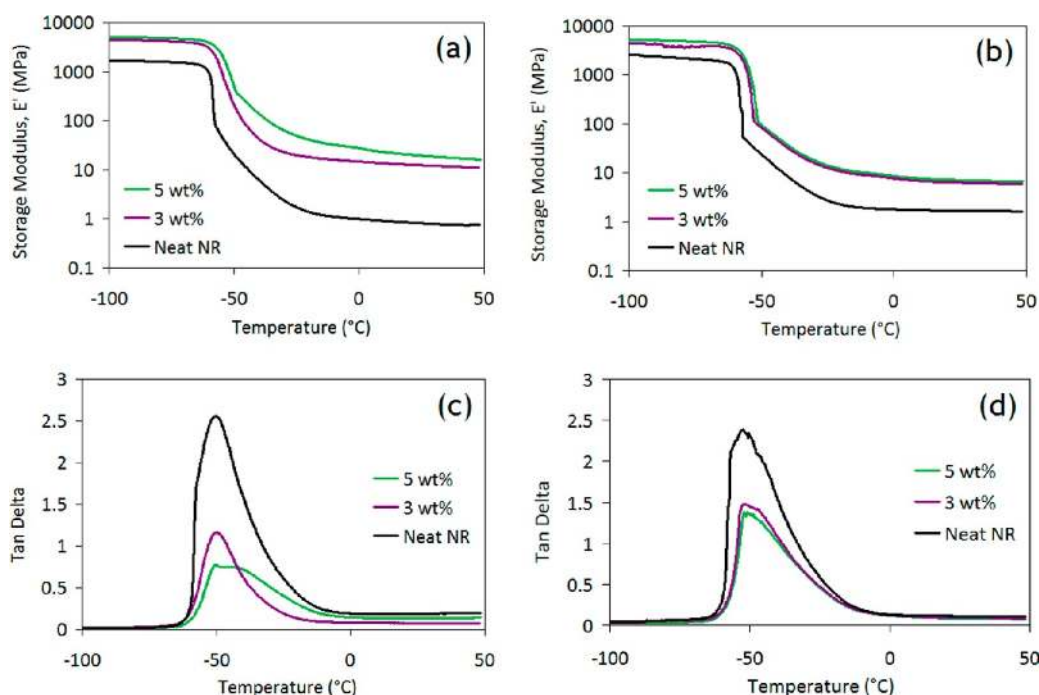


**Figure 8.** DMA plots of storage modulus versus temperature for the (a) solution-treated and (b) milled RG-O/NR nanocomposites. Graphs (c) and (d) show plots of  $\tan \delta$  versus temperature for the solution-treated and milled nanocomposites, respectively.

variation in fracture toughness with loading was observed, but in both cases the 3 wt % samples showed the highest energy to break of the loadings tested (see Supporting Information, Figure S.14).

Results from DMA temperature scans are shown in Figure 8, and a tabular summary is provided in Table S.1. Larger increases in storage modulus ( $E'$ ) were observed in the solution-treated samples compared with the milled samples, although the significant difference in moduli observed between the milled and solution-treated compounds in tensile testing was not reflected in the glassy moduli measured by DMA. As expected, increases in  $E'$  as well as disparities in  $E'$  between the two sample types became much more significant above the glass transition ( $T_g$ ), as the modulus contrast between the polymer and filler (network) increases by several orders of magnitude. Comparing the storage moduli of 5 wt % nanocomposites to neat NR (Table S.1), the modulus increased

by a factor of 3.4 and 2 at  $-100^\circ\text{C}$ , but by factors of 19.5 and 4.7 at  $25^\circ\text{C}$  for the solution-treated and milled nanocomposites, respectively. Strain sweeps of the nanocomposites at  $25^\circ\text{C}$  showed a progressive decrease in the limiting linear strain with increasing RG-O loading, with a sharp decrease in limiting strain at 4 wt % for the milled nanocomposites, coinciding with the onset of electrical percolation. This is the so-called “Payne effect”<sup>21</sup> as known in the rubber industry and more generally characteristic of filled composite melts,<sup>22–24</sup> largely due to perturbation and breakdown of filler networks.<sup>25–27</sup> However, the solution-treated samples were significantly more strain sensitive than the milled samples, supporting the existence of a more highly connected filler network in the former type (see Figure S.15).

Analysis of  $\tan \delta$  and loss modulus ( $E''$ ) peaks showed little to no change in  $T_g$  with loading; however, the shape and height of the peak changed significantly with incorporation of



RG-O platelets. For both the solution-treated and milled nanocomposites, a reduction in the height and breadth of the  $\tan \delta$  peak was observed. This suggests that RG-O has effectively immobilized NR chains near the polymer–particle interface due to favorable interfacial interactions with the NR matrix,<sup>1</sup> supporting the notion that favorable interfacial bonding exists in this system given the similarities in surface chemistry between RG-O and carbon black.<sup>28,29</sup> The decrease in the  $\tan \delta$  peak amplitude was more significant for the solution treated nanocomposites—decreasing by approximately 70% and 38% for the solution treated and milled 5 wt % nanocomposites, respectively—which is the result of the large difference in  $E'$  between the two sample types near and above the transition zone.

## 7. DISCUSSION ON MECHANICAL PROPERTIES

Mechanisms of reinforcement are strongly influenced by the dispersion morphology. While in both sets of nanocomposites the platelets were well-exfoliated with a high aspect ratio (see section 8), in the solution-treated compounds most of the platelets were arranged in a connected network structure formed within the interstitial areas between latex particles, promoting the formation of an elastic network of filler which greatly increased the stiffness of the compound. In addition, the stark difference in elasticity of the solution-treated and milled compounds may be due to the clustering of RG-O platelets in the interstitial areas between particles, preventing the interparticle diffusion of chains which provides cohesion between the latex particles. Thus, we postulate that the weblike network morphology promotes formation of a sample-spanning elastic filler network which greatly increases stiffness, but which compromises the elongation performance by preventing welding of the interfaces between some of the latex particles.<sup>30</sup>

By contrast, the milled samples had a more homogeneous and uniform dispersion corresponding to the more “ideal” nanocomposite morphology. At low strains simple shear lag effects<sup>31</sup> result in significant initial modulus enhancement; at higher strains the uniformly dispersed high aspect ratio RG-O platelets seemed to promote strain-induced crystallization of NR, as suggested by the Mooney–Rivlin plots in Figure 9

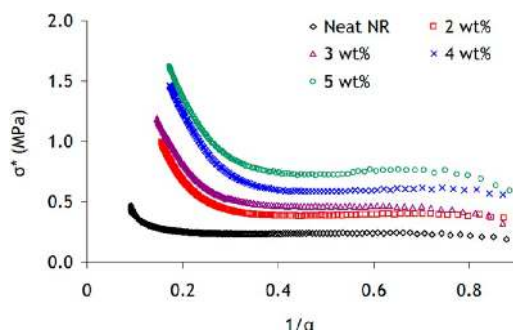


**Figure 9.** Mooney–Rivlin plots of the stress–strain curves shown in Figure 5a, showing the progressive shifting of the onset of strain-induced crystallization to lower strains with increasing RG-O loading.

showing the shifting of the upturn in the curves to higher  $1/\alpha$  values (thus lower strains) with increasing RG-O loading. Mooney–Rivlin analysis suggests that the crystallization process begins at progressively lower strains as the RG-O loading is increased. This conclusion is in agreement with recent work by Ozbas and co-workers, who investigated strain-

induced crystallization of thermally exfoliated graphite oxide/NR nanocomposites<sup>4</sup> and, based on the ideas of Mullins and Tobin,<sup>32</sup> concluded that the large interfacial surface area of the platelets led to a pronounced strain amplification effect that promoted an early onset of strain-induced crystallization. Thus, modulus enhancement in the milled samples may be due to a combination of mechanical restraint by high aspect ratio platelets,<sup>31</sup> alignment of platelets during stretching, and promotion of strain-induced crystallization by the RG-O platelets.

It may be noted that the modulus and strength enhancements achieved with RG-O in this study are comparable to those achieved with much higher loadings of carbon black in the literature.<sup>32</sup> Similar results have been reported for other nanofillers as well, such as organoclays.<sup>33</sup> It is not the aim of this article to directly compare property enhancements with carbon black to RG-O, although our results in a separate study<sup>34</sup> show that the difference in property enhancement between graphene fillers and carbon black is heavily contingent upon both the type of graphene-based material and the dispersion method. The superior reinforcement capability of graphene-based materials likely results from a combination of the mechanisms described above—higher aspect ratio, alignment during stretching, and promotion of strain-induced crystallization. The higher aspect ratio structure of graphene is also the likely reason for the significantly lower electrical percolation threshold observed in the milled nanocomposites in this study, compared to conventional carbon black-filled compounds.<sup>35</sup>

## 8. QUANTIFYING DISPERSION: AN ANALYSIS OF COMPOSITE MODELS AND TEM MICROGRAPHS

A variety of micromechanical models have been developed to analyze and predict the mechanical properties of polymer composites when filled with particles of a known geometry.<sup>36</sup> Typical parameters in such models include the moduli of the matrix and filler, the volume fraction of filler, and a filler shape factor (e.g., aspect ratio). Some of these models provide analytical, closed form predictions of composite modulus based on these parameters allowing them to be easily used (see Supporting Information), but many assumptions are required in their development, such as perfect interfacial adhesion and idealized filler geometries. These assumptions become more severe when these models are extended to the domain of polymer nanocomposites as particle–particle effects are ignored, and the properties of the matrix polymer are assumed to be independent of the filler, despite evidence for a perturbation in polymer dynamics near a particle interface (the “interphase”).<sup>37–39</sup> However, Fornes and Paul and others have shown that despite these simplifications, basic micromechanical models can effectively predict the properties of nanoclay/polymer nanocomposites.<sup>31</sup>

While the basic models considered in this work have similar predictive power, not all share the same conceptual foundation nor the same assumptions in their derivation. For example, Mori and Tanaka’s model<sup>40</sup> was initially developed to describe the effect of inclusions in a metal based on Eshelby’s solution to the equivalent inclusion problem; Tandon and Weng<sup>41</sup> extended Mori and Tanaka’s model to describe a polymer composite and validated the model with experimental data. On the other hand, the widely used Guth equation to describe the elastic modulus of filled elastomers evolved from Smallwood’s expression for the viscosity of filled liquids and considers only

hydrodynamic contributions to reinforcement by spherical or rodlike inhomogeneities.<sup>42,43</sup> It is not the aim of this section to review or compare differences in the theoretical underpinnings of these models, as that has been covered elsewhere in detail.<sup>36</sup> Rather, the goal of this section is to select a few of the most widely used models from the literature and compare their effectiveness in predicting the modulus of elastomers reinforced with graphene-based fillers or for quantifying filler dispersion in graphene–elastomer systems in terms of an average aspect ratio parameter,  $A_f$ .

An important component of most composite models is the modulus of the filler, which is challenging to determine for nanomaterials such as graphene.<sup>44</sup> Two studies have reported on the modulus of graphene platelets derived from GO.<sup>45,46</sup> In one study, the modulus was found to be inversely proportional to the C:O ratio of the material; monolayer graphene oxide sheets exhibited a modulus of 650 GPa, while reduced graphene oxide had a modulus of 250 GPa.<sup>45</sup> In another report, graphene oxide was reported to have a modulus of 208 GPa, and no difference in modulus was reported between single and double-layer platelets at small strains. For the purposes of this analysis, 250 GPa was used as an estimate of the RG-O platelet stiffness. However, it should be noted that for this system variations in the filler modulus have little influence on the predictions of the models. As pointed out by Kim and co-workers,<sup>47</sup> a plateau effect is predicted by the models as the ratio of filler to matrix modulus is increased beyond  $\sim 10^4$  (assuming all other parameters held constant), a condition met by many graphene/elastomer composite systems including the one in this study. The filler modulus is not used in the Guth equation and will thus have no effect on its predictions; see Supporting Information for relevant equations.

For the calculations, values of the platelet shape factor or aspect ratio were varied in each model to achieve best fit to the data, as commonly performed in the literature in an attempt to quantify filler dispersion in terms of the shape factor. Best fit curves to the data were generated, then the aspect ratio  $A_f$  (or shape factor  $f$ , in the case of the Guth model) was used as the independent parameter in the model and adjusted until the model prediction coincided with the line of best fit to the data points. The modified Halpin–Tsai model incorporates the maximum packing volume fraction  $\phi_m$  of the filler as a parameter and was taken as 0.05 for RG-O platelets of nominal  $A_f > 200$  based upon the treatise of Bicerano and co-workers,<sup>48</sup> as described in the Supporting Information. The results of the curve fittings are summarized in Table 1. The Mori–Tanaka

**Table 1. Predictions of Filler Anisotropy—Aspect Ratio,  $A_f$ , or Shape Factor,  $f$ —by Basic Composite Models**

model	$A_f$ or $f$
Mori–Tanaka	115
Halpin–Tsai	89
modified Halpin–Tsai	53
Guth–Gold	44

and Halpin–Tsai models predicted similar  $A_f$  values, showing large deviations from the data at higher loadings. The modified Halpin–Tsai model and Guth equation captured the trends in the data much more accurately, with a nonlinear increase in modulus as a function of  $\phi$ . The shape factor in the Guth equation is also an aspect ratio but is defined for a rodlike

inhomogeneity,<sup>43</sup> and fitting to the data predicts a shape factor  $f$  of 44.

To evaluate the effectiveness of the models, the predicted  $A_f$  or  $f$  was compared against the value determined from TEM analysis. In this work, following a procedure described by Fornes and Paul,<sup>31</sup> average values of  $A_f$  were obtained from several representative TEM micrographs of 5 wt % green and milled composite samples. The procedure is illustrated in Figure S.18 and consists of converting the micrograph to a binary image to isolate the platelets from the background and then performing a shape analysis on each platelet following a spatial calibration of the micrograph. The software allows particle size to be analyzed in a variety of ways allowing for the platelet dimensions and thus average aspect ratio to be determined. It should be noted that the average value of aspect ratio determined by TEM analysis can vary significantly depending on the measurements of platelet size used in the software; these issues are discussed at length in the Supporting Information. Briefly, each particle was modeled as an effective rectangle; the perimeter (measured by the software) was approximated to be half the length of each particle while the thickness was calculated from the length and measured particle area.

A normalized histogram of particle  $A_f$  values determined from three different TEM micrographs of milled and green 5 wt % RG-O/NR nanocomposites is shown in Figure 10. The

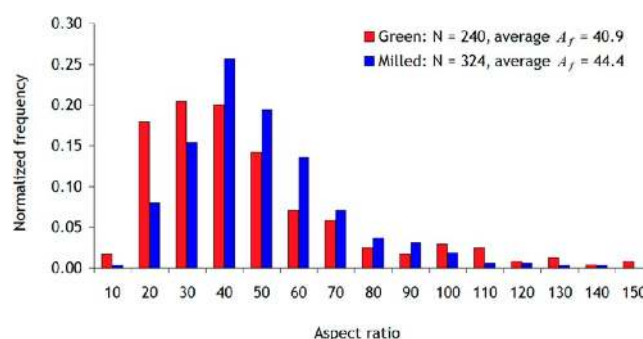


**Figure 10.** Histogram of aspect ratio ( $A_f$ ) values for green and milled RG-O/NR nanocomposites as determined from TEM micrographs.

average  $A_f$  of the milled nanocomposites was found to be higher than for the green nanocomposites, suggesting an improvement in dispersion with milling. A considerably larger amount of low- $A_f$  tactoids ( $A_f < 20$ ) was observed in the green composite micrographs. Assuming these micrographs to be truly representative of the sample dispersion, the difference may be attributed to the milling process driving further exfoliation of multilayer tactoids. However, the higher frequency of low aspect ratio platelets in the green sample micrographs could be due to errors in identifying individual platelets. For instance, given the larger amount of platelet–platelet interaction evident from the green sample micrographs, there would be a greater probability of misidentifying two individual platelets as one thicker platelet.<sup>31</sup>

Comparing the values of  $A_f$  in Table 1 with the data shown in Figure 10, it appears that the Guth model provides the best results if the shape factor is interpreted directly as the aspect ratio of the platelets. In addition, the Guth equation captures the trend in reinforcement as a function of loading more effectively than the other models. Figure 11 compares the predictions of the four models using a shape factor or aspect



ratio of 44 as determined by TEM analysis; the excellent agreement between the Guth model and the data is evident. The predictions of both the Mori–Tanaka and Halpin–Tsai models differ from the  $A_f$  determined by microscopy by a factor of 2 or more, while the modified Halpin–Tsai model provides a much closer estimate.

A similar analysis of composite models was conducted on nanoclay/rubber nanocomposites by Wu and co-workers,<sup>51</sup> who reported that the models overpredicted the modulus trends in the experimental data. To address this disparity, a filler “modulus reduction factor” was incorporated into the models in attempt to account for the effects of imperfect interfacial bonding,<sup>52</sup> disorientation/misalignment to the tensile axis, multilayer tactoids, etc. According to their analysis, a factor of  $\sim 0.66$  established a better agreement between the model predictions and experimental data, using the  $A_f$  values determined from TEM directly in the models. However, the results shown above suggest that no reduction factor is necessary for this system—all the models considered here either predict close to or below the experimental data when using  $A_f$  as determined by TEM, obviating the need for any such reduction factor which would simply increase the disagreement between the models and the data. Rather than arbitrarily adjusting the value of the platelet modulus, we speculate that more accurate or careful determinations of  $A_f$  by TEM could lead to better agreement between the Mori–Tanaka and (modified) Halpin–Tsai models, as other analysis methods suggest the  $A_f$  quantified by TEM is likely quite different from the “true” average  $A_f$  of the dispersed platelets.

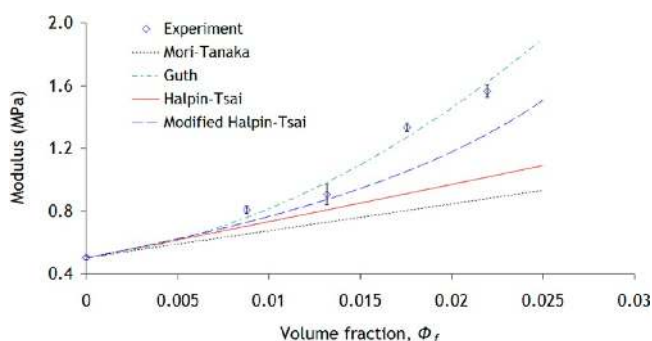


**Figure 11.** Comparison between the experimental modulus data of the milled RG-O/NR nanocomposites and predictions of the composite models, taking  $A_f = 44$  as determined by TEM analysis.

SEM micrographs of isolated RG-O platelets (see Figure S.5) can allow estimation of platelet lateral dimensions following a similar procedure with the TEM micrographs; estimates of aspect ratio by SEM require assumption of platelet thickness which cannot be determined from SEM micrographs. Comparison of the average lateral dimension (not  $A_f$ ) of the platelets as determined by TEM with the average diameter of the platelets observed in SEM micrographs reveals very different estimates of the average platelet size and distribution of sizes as shown in Figure S.20. The average platelet lateral dimension was 277 nm by SEM, while just 114 nm based on TEM analysis of the nanocomposite sections (milled samples). The disparity could be due to several factors, most notably the irregular particle shape which makes it unlikely that the full width of the platelet would be directly visible and edge-on to the beam, and may not reflect actual changes in the dimensions of the platelets due to, e.g., particle attrition.<sup>44</sup> Even taking into

account imperfect interfacial bonding<sup>52</sup> as well as other issues in quantifying dispersion from TEM micrographs,<sup>31</sup> the TEM quantification procedure likely underestimates  $A_f$  and thus the modified Halpin–Tsai model may indeed provide a closer estimate of the nanocomposite modulus based on the “true” particle aspect ratio. As will be shown in an upcoming paper,<sup>34</sup> the surface chemistry of the filler can have a significant effect on modulus enhancement, and thus for other fillers such as nanoclays or graphene oxide, modulus reduction factors may be more appropriate as interfacial bonding between the filler and matrix becomes weaker.

Finally, this work highlights the fact that one must be cautious in the interpretation of the  $A_f$  value determined from composite theory analysis of modulus data or other physical property measurements. All of these models assume a uniform dispersion of filler and when particle–particle interactions become significant, such as in the case of the solution treated or green compounds, the use of an  $A_f$  parameter from composite models to quantify the “quality” of the dispersion becomes questionable. Following the same procedure to analyze the experimental modulus data from the solution-treated compounds,  $A_f$  predictions from the Mori–Tanaka and Halpin–Tsai models based on the fitting procedure described above were 1295 and 790, respectively. None of these models accurately modeled the trends in modulus with loading observed in the experimental data, and all predict unreasonably large aspect ratio values. The Guth equation was able to capture the trends in modulus much more effectively, but still overestimated the filler anisotropy ( $f = 155$ ). While composite theory predicts a higher aspect ratio for the solution-treated samples, TEM and WAXS evidence suggests that  $A_f$  of the solution treated samples was lower than the milled samples. Thus, these models can be used to fit to the data by adjusting  $A_f$  or  $f$  indiscriminately, but as expected they cannot be used to quantify dispersion in any meaningful way in the case of a network morphology with significant particle–particle interaction. In the case of the homogeneous dispersion, the models provide a much more accurate quantification of dispersion, and indeed with the Guth equation, the predictions are very close to the experimental data. Moreover, the agreement between these models and the experimental data, along with the small change in  $T_g$  and Mooney–Rivlin analysis, suggests that reinforcement in the well-dispersed milled nanocomposites is largely due to two mechanisms: mechanical restraint—i.e., due to the high modulus and aspect ratio of the RG-O platelets rather than a perturbation in the properties of the rubber matrix<sup>31</sup>—as well as promotion of strain-induced crystallization by the high aspect ratio RG-O platelets.

## 9. CONCLUSIONS

Nanocomposites of RG-O platelets in a NR matrix were prepared by latex co-coagulation and then processed (to incorporate curing agent) by one of two methods: solution treatment or two-roll milling. It was demonstrated that the processing approach had a tremendous impact on the composite morphology and thus properties. Solution treatment (implantation of peroxide curing agent by swelling the NR in toluene) preserved the segregated filler network morphology produced by the co-coagulation procedure, whereas the milling process destroyed this network and generated a homogeneous dispersion of RG-O platelets in the NR matrix. The segregated network morphology was shown to be advantageous for conductivity properties and greatly increased the stiffness of the

composite versus neat NR, but also significantly reduced the elongation to break the samples. The milled nanocomposites also exhibited enhanced stiffness and strength while maintaining a high elongation to break. We proposed that reinforcement in the solution-treated or green nanocomposites is due to formation of a sample-spanning network of strongly interacting RG-O platelets located in the interstitial regions between latex particles, whereas in the milled nanocomposites, reinforcement is due to simple mechanical restraint (i.e., modulus contrast between the polymer and well-dispersed filler) along with promotion of strain-induced crystallization by the high aspect ratio RG-O platelets.

The property changes with filler loading were analyzed using basic composite models established in the literature. The dispersion of filler for both sets of composite samples was quantified using models describing elastic modulus. In general, since property improvements changed more dramatically with filler loading in the case of the solution-treated composites, a better dispersion (higher  $A_f$ ) was predicted for these samples. However, quantifying dispersion by these models is not particularly meaningful in this instance, since the dispersion is highly nonideal. It was indeed shown that there were significant discrepancies between the dispersion as quantified by TEM and the dispersion quantified by composite theory in the case of the solution-treated samples. On the other hand, the composite models—in particular the Guth model—appeared to offer much more reasonable estimates of  $A_f$  (or  $f$ ) for the milled nanocomposites, which had a uniform and homogeneous filler dispersion. For samples processed on the mill, application of the Guth model or modified Halpin–Tsai model may provide meaningful and useful predictions for engineering purposes of modulus and/or quantifications of filler dispersion although a discrepancy appears to exist between the particle size determined by TEM and other methods.

The core focus of this work was on the significant impact that processing can have on morphology and properties. The property measurements on the milled RG-O/NR nanocomposites should be of significant interest from a technological perspective, as latex co-coagulation of nanocomposites followed by milling parallels the masterbatch processing approach that could be used industrially. The properties of the solution-treated nanocomposites—with their low percolation threshold and low modulus, semicrystalline thermoplastic-like mechanical properties—could be of interest in their own right for certain applications.

## ■ ASSOCIATED CONTENT

### ■ Supporting Information

SEM images of fracture sections, latex particles and RG-O platelets, supplementary TEM images, X-ray spectra, properties of uncured nanocomposites, additional stress–strain and DMA data, dependence of mechanical properties on DCP concentration and curing time, and details of TEM quantification procedure. This material is available free of charge via the Internet at <http://pubs.acs.org>.

## ■ AUTHOR INFORMATION

### Corresponding Author

\*E-mail: [r.ruoff@mail.utexas.edu](mailto:r.ruoff@mail.utexas.edu).

### Notes

The authors declare no competing financial interest.

## ■ ACKNOWLEDGMENTS

The authors thank D. R. Paul for use of the two-roll mill and hot press, K. M. Liechti for assistance with and use of the MTS machine for stress–strain testing, W. Li and X. Kim for DMA use, C. Pulford and X. Yang at Goodyear for helpful advice, and D. Romanovicz for cryomicrotome training. This project was funded in part by the Goodyear Tire and Rubber Company and by the Laboratory Directed Research and Development (LDRD) program and the National Institute for Nano-Engineering at Sandia National Laboratories.

## ■ REFERENCES

- (1) Galimberti, M. *Rubber-Clay Nanocomposites*; John Wiley & Sons: Hoboken, NJ, 2011.
- (2) Potts, J. R.; Dreyer, D. R.; Bielawski, C. W.; Ruoff, R. S. *Polymer* **2011**, *52*, 5–25.
- (3) Ozbas, B.; O'Neill, C. D.; Register, R. A.; Aksay, I. A.; Prud'homme, R. K.; Adamson, D. H. *J. Polym. Sci., Part B: Polym. Phys.* **2012**, *50*, 910–916.
- (4) Ozbas, B.; Toki, S.; Hsiao, B. S.; Chu, B.; Register, R. A.; Aksay, I. A.; Prud'homme, R. K.; Adamson, D. H. *J. Polym. Sci., Part B: Polym. Phys.* **2012**, *50*, 718–723.
- (5) Zhan, Y. H.; Wu, J. K.; Xia, H. S.; Yan, N.; Fei, G. X. *Macromol. Mater. Eng.* **2011**, *296*, 590–602.
- (6) Li, D.; Muller, M. B.; Gilje, S.; Kaner, R. B.; Wallace, G. G. *Nat. Nanotechnol.* **2008**, *3* (2), 101–105.
- (7) Park, S.; An, J. H.; Jung, I. W.; Piner, R. D.; An, S. J.; Li, X. S.; Velamakanni, A.; Ruoff, R. S. *Nano Lett.* **2009**, *9* (4), 1593–1597.
- (8) Park, S.; Ruoff, R. S. *Nat. Nanotechnol.* **2009**, *5* (4), 217–224.
- (9) Zhang, L.; Wang, Y.; Wang, Y.; Sui, Y.; Yu, D.-S. *J. Appl. Polym. Sci.* **2000**, *78* (11), 1873–1878.
- (10) Wang, Y.; Zhang, L.; Tang, C.; Yu, D.-S. *J. Appl. Polym. Sci.* **2000**, *78* (11), 1879–1883.
- (11) Wu, Y.-P.; Wang, Y.-Q.; Zhang, H.-F.; Wang, Y.-Z.; Yu, D.-S.; Zhang, L.-Q.; Yang, J. *Compos. Sci. Technol.* **2005**, *65*, 1195–1202.
- (12) Varghese, S.; Karger-Kocsis, J. *Polymer* **2003**, *44*, 4921–4927.
- (13) Valadares, L. F.; Leite, C. A. P.; Galembeck, F. *Polymer* **2006**, *47* (2), 672–678.
- (14) Pojanavaraphan, T.; Magaraphan, R. *Eur. Polym. J.* **2008**, *44* (7), 1968–1977.
- (15) White, J. L. *Rubber Processing: Technology - Materials - Principles*; Hanser/Gardner: Cincinnati, OH, 1995.
- (16) Mullins, L. *Rubber Chem. Technol.* **1969**, *42*, 339–362.
- (17) Bauhofer, W.; Kovacs, J. Z. *Compos. Sci. Technol.* **2009**, *69* (10), 1486–1498.
- (18) Busse, W. F. *Ind. Eng. Chem. Res.* **1931**, *24* (2), 140–146.
- (19) Mark, J. E.; Erman, B.; Eirich, F. R. *The Science and Technology of Rubber*, 3rd ed.; Elsevier: Amsterdam, 2010.
- (20) Wood, L. A.; Bullman, G. W. *J. Polym. Sci.* **1972**, *10*, 43–50.
- (21) Payne, A. R. *J. Appl. Polym. Sci.* **1962**, *6* (19), 57–63.
- (22) Potts, J. R.; Murali, S.; Zhu, Y.; Zhao, X.; Ruoff, R. S. *Macromolecules* **2011**, *44*, 6488–6495.
- (23) Kim, H.; Macosko, C. W. *Macromolecules* **2008**, *41* (9), 3317–3327.
- (24) Krishnamoorti, R.; Yurekli, K. *Curr. Opin. Colloid Interface Sci.* **2001**, *6*, 464–470.
- (25) Bokobza, L. *Macromol. Mater. Eng.* **2004**, *289*, 607–621.
- (26) Wang, X.; Roberston, C. G. *Phys. Rev. E: Stat., Nonlinear, Soft Matter Phys.* **2005**, *72*, 031406.
- (27) Voet, A. *J. Polym. Sci., Part D: Macromol. Rev.* **1980**, *15*, 327–373.
- (28) Donnet, J.-B.; Voet, A. *Carbon Black: Physics, Chemistry, and Elastomer Reinforcement*; Marcel Dekker: New York, 1976; p 351.
- (29) Dreyer, D. R.; Park, S.; Bielawski, C. W.; Ruoff, R. S. *Chem. Soc. Rev.* **2010**, *39* (1), 228–240.
- (30) Steward, P. A.; Hearn, J.; Wilkinson, M. C. *Adv. Colloid Interface Sci.* **2000**, *86*, 195–267.

- (31) Fornes, T. D.; Paul, D. R. *Polymer* **2003**, *44* (17), 4993–5013.
- (32) Mullins, L.; Tobin, N. R. *J. Appl. Polym. Sci.* **1965**, *9*, 2993–3009.
- (33) Arroyo, M.; Lopez-Manchado, M. A.; Herrero, B. *Polymer* **2003**, *44* (8), 2447–2453.
- (34) Potts, J. R.; Shankar, O.; Murali, S.; Du, L.; Ruoff, R. S. *Personal communication*, 2012.
- (35) Nan, C.-W.; Shen, Y.; Ma, J. *Annu. Rev. Mater. Res.* **2010**, *40*, 131–151.
- (36) Tucker, C. L.; Liang, E. *Compos. Sci. Technol.* **1999**, *59*, 655–671.
- (37) Ellison, C. J.; Torkelson, J. M. *Nat. Mater.* **2003**, *2* (10), 695–700.
- (38) Bansal, A.; Yang, H.; Li, C.; Cho, K.; Benicewicz, B. C.; Kumar, S. K.; Schadler, L. S. *Nat. Mater.* **2005**, *4* (9), 693–698.
- (39) Rittigstein, P.; Priestley, R. D.; Broadbelt, L. J.; Torkelson, J. M. *Nat. Mater.* **2007**, *6* (4), 278–282.
- (40) Mori, T.; Tanaka, K. *Acta Metall.* **1973**, *21*, 571–574.
- (41) Tandon, G. P.; Weng, G. J. *Polym. Compos.* **1984**, *5*, 327–333.
- (42) Bergström, J. S.; Boyce, M. C. *Rubber Chem. Technol.* **1999**, *72* (4), 633–656.
- (43) Guth, E. *J. Appl. Phys.* **1945**, *16* (20), 20–25.
- (44) Paul, D. R.; Robeson, L. M. *Polymer* **2008**, *49* (15), 3187–3204.
- (45) Gómez-Navarro, C.; Burghard, M.; Kern, K. *Nano Lett.* **2008**, *8* (7), 2045–2049.
- (46) Suk, J. W.; Piner, R. D.; An, J.; Ruoff, R. S. *ACS Nano* **2010**, *4*, 6557–6564.
- (47) Kim, H.; Abdala, A. A.; Macosko, C. W. *Macromolecules* **2010**, *43*, 6515–6530.
- (48) Bicerano, J.; Douglas, J. F.; Brune, D. A. *J. Macromol. Sci., Polym. Rev.* **1999**, *39* (4), 561–642.
- (49) King, J. A.; Via, M. D.; Morrison, F. A.; Wiese, K. R.; Beach, E. A.; Cieslinski, M. J.; Bogucki, G. R. *J. Compos. Mater.* **2011**, DOI: 10.1177/0021998311414073.
- (50) Fisa, B.; Vu-Khanh, T.; Remillard, B. *J. Thermoplast. Compos.* **1988**, *1*, 361–370.
- (51) Wu, Y.; Jia, Q.; Yu, D.-S.; Zhang, L. *Polym. Test.* **2004**, *23*, 903–909.
- (52) Shia, D.; Hui, C. Y.; Burnside, S. D.; Giannelis, E. P. *Polym. Compos.* **1998**, *19* (5), 608–617.